SCIENCE CHINA
Chemistry

•ARTICLES•

https://doi.org/10.1007/s11426-024-2536-8

Intermarriage of $InVO_4$ and $BiVO_4$ via cation-exchange to boost charge separation for efficient photocatalytic CH_4 oxidation to oxygenates

Guang-Xing Dong[†], Meng-Ran Zhang[†], Cheng-Cheng Jiao, Zhao-Lei Liu, Ke Su, Min Zhang[*] & Tong-Bu Lu[*]

MOE International Joint Laboratory of Materials Microstructure, Institute for New Energy Materials and Low Carbon Technologies, School of Materials Science and Engineering, Tianjin University of Technology, Tianjin 300384, China

Received November 29, 2024; accepted January 18, 2025; published online February 24, 2025

Achieving efficient and highly selective conversion of CH_4 into high-value-added chemicals through photodriving under mild conditions remains a significant challenge, primarily due to the limited utilization efficiency of photogenerated carriers. Herein, we report an *in-situ* growth strategy for constructing a robust $InVO_4$-based heterojunction by intermarrying $InVO_4$ and $BiVO_4$ through cation-exchange. This method enables the resultant $InVO_4/BiVO_4$ heterojunction to possess strong interfacial electronic coupling, which accelerates the interface charge transfer and significantly enhances the separation efficiency of photogenerated carriers. Under visible light-driven reaction conditions at ambient temperature and pressure, the $InVO_4/BiVO_4$ heterojunction demonstrates high selectivity (>90%) in photocatalyzing the oxidation of CH_4 to high-value oxygenated hydrocarbons (CH_3OH and HCHO), with a yield of 318.9 μmol g^{-1} h^{-1}, which is 4.8 times higher than that of pristine $BiVO_4$. Comprehensive control and isotope tracing experiments, as well as *in-situ* detection of transient species reveal that the key intermediate product CH_3OOH is primarily formed through the binding of $\cdot CH_3$ radicals with protons and O_2, explaining why the oxygen source of the CH_3OH product is mainly derived from O_2.

cation-exchange, CH_4 conversion, charge separation, photocatalysis, vanadate

Citation: Dong GX, Zhang MR, Jiao CC, Liu ZL, Su K, Zhang M, Lu TB. Intermarriage of $InVO_4$ and $BiVO_4$ via cation-exchange to boost charge separation for efficient photocatalytic CH_4 oxidation to oxygenates. *Sci China Chem*, 2025, 68, https://doi.org/10.1007/s11426-024-2536-8

1 Introduction

Natural gas has emerged as a prominent economic resource of the 21st century, distinguished by its continually expanding proven reserves and increasing extraction rates. However, methane (CH_4), the primary component of natural gas, exhibits a greenhouse effect significantly more potent than CO_2 [1,2]. If CH_4 can be efficiently converted into high-value products under mild conditions, it would not only enhance its utilization value but also alleviate the substantial costs and potential climate and environmental issues associated with natural gas transportation [3,4]. Nevertheless, the chemical inertia of the C–H bonds poses a significant challenge for achieving direct conversion of CH_4 under mild conditions [5–8]. Currently, the high-efficiency catalysts used for the direct conversion of CH_4 are mostly rare and expensive noble metals such as platinum and palladium, and the reaction conditions often require high-energy inputs like high temperatures and high pressures. This is far from achieving the desired scalability and economy for CH_4 conversion in industry [9–14]. The replacement of traditional thermal catalysis with photocatalysis for the oxidation of CH_4 to high-value-added products under mild conditions

†Equally contributed to this work.
*Corresponding authors (email: zm2016@email.tjut.edu.cn; lutongbu@tjut.edu.cn)

signifies a highly promising and emerging green technology [15–18].

In recent years, a diverse array of photocatalysts (such as TiO_2, ZnO, $BiVO_4$, and CeO_2) have been developed to achieve photocatalytic oxidation of CH_4 into high-value-added products [19–28]. Nonetheless, these photocatalysts often suffer from low photocatalytic efficiency [29–31], due to the contradiction between the thermodynamic driving force required for the reaction and their light-harvesting capabilities, as well as the issue of severe carrier recombination. Additionally, the oxidation products derived from CH_4 are more prone to further oxidation than CH_4 itself, leading to excessive oxidation and compromised selectivity of the desired products. Among the numerous semiconductor photocatalysts developed, $BiVO_4$ is widely used in photocatalytic CH_4 oxidation due to its excellent visible light absorption and photo-oxidation capabilities [32]. However, pure $BiVO_4$ is hampered by severe photogenerated carrier recombination and limited reduction ability stemming from its overly positive reduction potential, leading to low photocatalytic activity for CH_4 oxidation [33]. Combining $BiVO_4$ with other semiconductors that possess a strong reducing ability to construct a Z-scheme heterojunction can enhance its reducing ability while improving the efficiency of photogenerated carrier separation [34,35]. Nevertheless, the interfaces of heterojunctions fabricated through traditional techniques, such as electrostatic self-assembly and *in-situ* deposition, lack the necessary tightness, resulting in inefficient charge transfer at the interface.

To overcome this obstacle, we herein present an *in-situ* cation-exchange strategy for the construction of a $BiVO_4$-based direct Z-scheme heterojunction, by introducing Bi^{3+} ions onto an $InVO_4$ substrate to form $BiVO_4$ (Figure 1a). The resultant $InVO_4/BiVO_4$ heterojunction can not only preserve the excellent oxidation performance of $BiVO_4$ and the superior reduction ability of $InVO_4$, but also possess a strong interfacial electronic coupling due to the tightly bonded interface, significantly promoting the migration and separation of photogenerated carriers. As anticipated, the prepared $InVO_4/BiVO_4$ heterojunction can achieve efficient photocatalytic conversion of CH_4 into high value-added oxygenated hydrocarbons under room temperature, atmospheric pressure, and visible light irradiation, utilizing atmospheric oxygen as an oxidant. The yield of oxygenated hydrocarbon products for $InVO_4/BiVO_4$ reaches up to 318.9 μmol g^{-1} h^{-1} with a selectivity of 94.5%, far superior to that of $BiVO_4$ alone. Moreover, the photogenerated carrier separation pathways within $InVO_4/BiVO_4$, as well as the reaction mechanism of photocatalytic CH_4 oxidation, have been comprehensively elucidated by incorporating photophysical characterization, isotope-tracing experiments, and *in-situ* detection of transient species.

2 Results and discussion

2.1 Structural and morphological characterization

The crystal structures of the $InVO_4/BiVO_4$ composite, pris-

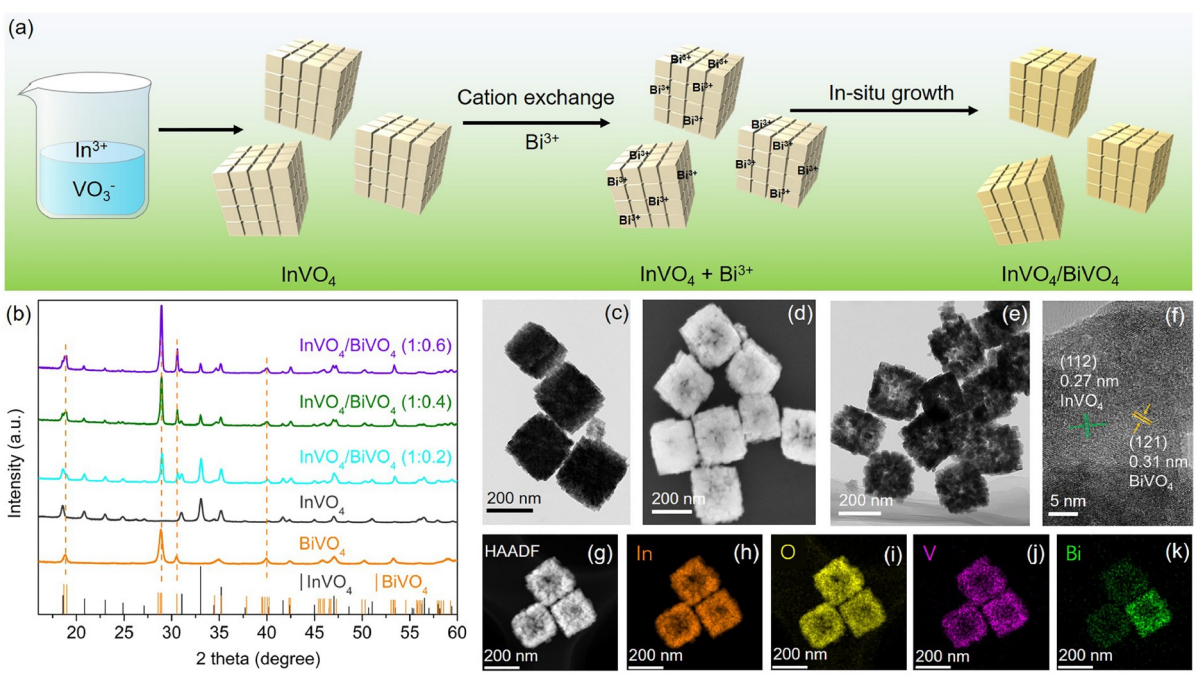

Figure 1 (Color online) (a) Schematic illustration of the preparation processes of $InVO_4/BiVO_4$. (b) XRD patterns of various photocatalysts. (c) TEM image of $InVO_4$. SEM (d), TEM (e), HRTEM (f), and HAADF-STEM (g) images of $InVO_4/BiVO_4$. (h–k) EDS mapping images (In, O, V, Bi) of $InVO_4/BiVO_4$.

tine $InVO_4$ and $BiVO_4$ were analyzed by X-ray diffraction (XRD) measurements. As depicted in Figure 1b, the characteristic diffraction peaks of the prepared $InVO_4$ substrate can be well matched with the orthorhombic phase of $InVO_4$ (JCPDS No. 48-0898), and the XRD pattern of pristine $BiVO_4$ reveals a monoclinic phase (JCPDS No. 14-0688). For the as-prepared $InVO_4/BiVO_4$ composite, apart from the distinct diffraction peaks of $InVO_4$, the diffraction peaks at 28.8°, 30.5°, and 40.2°, contributed by $BiVO_4$ can also be clearly identified. Their intensities are gradually enhanced with the increase in the introduced Bi^{3+} cation content, indicating the successful construction of the $InVO_4/BiVO_4$ composite through *in-situ* growth of $BiVO_4$ via cation-exchange, without altering the crystal structure of the $InVO_4$ substrate.

The transmission electron microscopy (TEM) and scanning electron microscopy (SEM) measurements revealed that the pristine $InVO_4$ exhibits a regular cubic morphology (200–300 nm) composed of small cubic nanoparticles (20–30 nm) (Figure 1c, Figure S1, Supporting Information online). The $InVO_4/BiVO_4$ composite, obtained by *in-situ* growth of $BiVO_4$ on $InVO_4$ substrate via cation-exchange strategy, still maintains the cubic structure with unchanged dimensions compared to pristine $InVO_4$ (Figure 1d, e). This indicates that the morphological characteristics of $InVO_4$ were preserved during the conversion process. High-resolution TEM (HRTEM) image of $InVO_4/BiVO_4$ shows that the prepared $InVO_4$ belongs to the orthorhombic phase, with a lattice spacing of 2.7 Å clearly observed for the (112) crystalline plane of $InVO_4$. Additionally, a lattice spacing of 3.1 Å, corresponding to the (121) crystalline plane of monoclinic phase $BiVO_4$, is also discernible in the HRTEM image of $InVO_4/BiVO_4$ (Figure 1f). Moreover, energy-dispersive X-ray spectroscopy (EDS) mapping measurements demonstrated that In, V and O elements are uniformly distributed on the $InVO_4$ substrate (Figure S2), while Bi elements are uniformly distributed throughout the $InVO_4/BiVO_4$ composite (Figure 1g–k, Figure S3), indicating that $BiVO_4$ in the $InVO_4/BiVO_4$ composite is evenly dispersed on the surface of the $InVO_4$ substrate. These results further confirmed the successful transformation and uniform loading of $BiVO_4$ on the $InVO_4$ substrate. The surface areas of the samples were obtained from the isothermal N_2 adsorption-desorption curves of $InVO_4/BiVO_4$, $InVO_4$ and $BiVO_4$. The results revealed that the surface area of the $InVO_4$ substrate exceeded that of $BiVO_4$, and the surface area of $InVO_4/BiVO_4$ was close to that of $InVO_4$ (Figure S4). This indicated that the structural characteristics of the $InVO_4$ substrate remained unchanged during the conversion process, which was consistent with the results of the TEM measurements. Additionally, the larger surface area was favorable for the catalyst to fully contact the reaction substrate, thereby enhancing catalytic activity.

High resolution X-ray photoelectron spectroscopy (XPS) measurements were further employed to investigate the interaction between $InVO_4$ and $BiVO_4$ in the as-prepared $InVO_4/BiVO_4$ composites. As depicted in the XPS survey spectrum of $InVO_4/BiVO_4$ (Figure S5), In, Bi, V, and O elements can be clearly identified. Notably, the binding energies of In 3d of the $InVO_4/BiVO_4$ sample exhibit a significant positive shift (~0.25 eV) compared to pure $InVO_4$, while the characteristic peaks of Bi 4f shift towards the lower binding energy by 0.30 eV compared to pristine $BiVO_4$ (Figure S6). Additionally, the binding energies of V 2p in the $InVO_4/BiVO_4$ composite fall between the corresponding binding energies of V 2p in pristine $InVO_4$ and $BiVO_4$ (Figure S7). These apparent changes in the binding energy imply a strong electronic coupling between $InVO_4$ and $BiVO_4$ in the $InVO_4/BiVO_4$ composite, indicating a closely contacted interface between $InVO_4$ and $BiVO_4$ via cation-exchange *in-situ* growth, which will facilitate interfacial charge transfer at the $InVO_4/BiVO_4$ interface. The direction of binding energy shifts of these elements indicates the occurrence of free electron transfer from $InVO_4$ to $BiVO_4$ during the *in-situ* growth of $BiVO_4$ on the $InVO_4$ substrate, ultimately leading to the formation of a built-in electric field directed from $InVO_4$ to $BiVO_4$.

2.2 Charge transport mechanism

To elucidate the underlying physical mechanisms responsible for the generation of the built-in electric field and the migration pathway of photogenerated carriers at the $InVO_4/BiVO_4$ interface, the energy band structures of $InVO_4$ and $BiVO_4$ were first evaluated by ultraviolet-visible diffuse reflectance spectrum (UV-vis DRS) measurements. As illustrated in Figure S8, both $InVO_4$ and $BiVO_4$ demonstrate a robust responsiveness within the visible light range. By analyzing the corresponding Tauc plots, the band gaps (E_G) of $InVO_4$ and $BiVO_4$ can be determined to be 2.08 and 2.15 eV (Figure S9), respectively, which align with previous reports on these materials [36,37]. Furthermore, the valence band (VB) edge potentials (E_{VB}) of $InVO_4$ and $BiVO_4$ were established to be 1.53 and 2.26 V (*vs*. SHE pH = 7), respectively, based on ultraviolet photoelectron spectroscopy (UPS) measurements (Figure 2a). Consequently, the conduction band (CB) edge potentials (E_{CB}) of $InVO_4$ and $BiVO_4$ can be calculated from the difference between E_G and E_{VB}, being −0.55 and 0.11 V *vs*. SHE, respectively, which are in close proximity to the flat-band potentials of $InVO_4$ and $BiVO_4$ derived from their Mott-Schottky plots (Figure S10). The resultant staggered energy structures between $InVO_4$ and $BiVO_4$ are illustrated in Figure 2b.

The Fermi levels of $InVO_4$ and $BiVO_4$ were further determined by UPS measurements, being −4.19 and −5.25 eV, respectively. When $BiVO_4$ grows *in-situ* on $InVO_4$ through

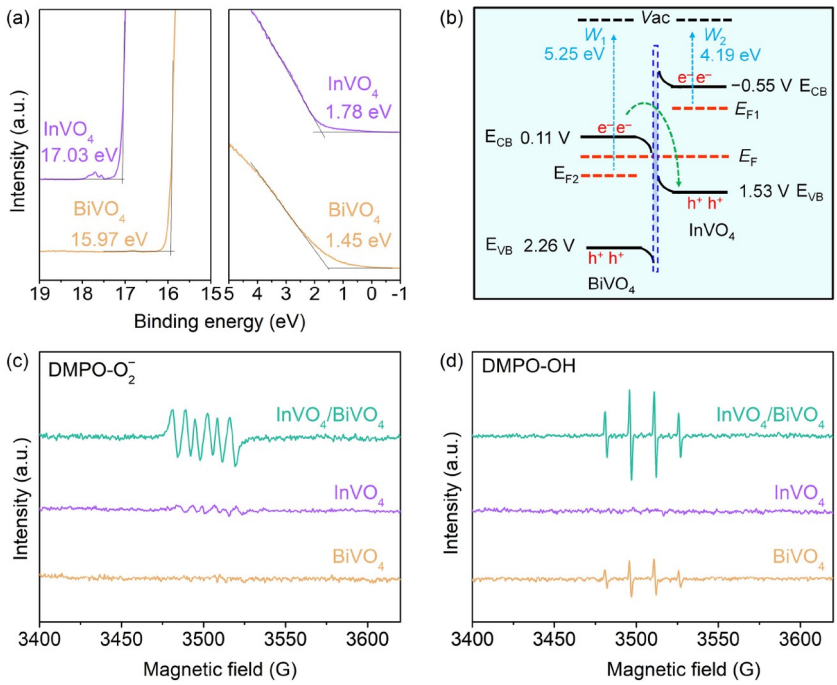

Figure 2 (Color online) (a) The UPS spectra of $InVO_4$ and $BiVO_4$. (b) Energy band structures of $InVO_4$ and $BiVO_4$, and the schematic illustration of the charge-transfer mechanism of the direct Z-scheme in $InVO_4/BiVO_4$. EPR spectra of (c) DMPO–O_2^- and (d) DMPO–OH for $InVO_4$, $BiVO_4$, and $InVO_4/BiVO_4$.

cation-exchange, the higher Fermi level of $InVO_4$ relative to $BiVO_4$ will drive the migration of free electrons from $InVO_4$ to $BiVO_4$, ultimately unifying the Fermi level of the entire system. This deduction is consistent with the results of the XPS analysis presented above. Additionally, the transfer of free electrons from $InVO_4$ to $BiVO_4$ will cause the energy bands of $InVO_4$ and $BiVO_4$ to bend upward and downward, respectively, as illustrated in Figure 2b. It is evident that the band bending of $InVO_4$ and $BiVO_4$, coupled with the built-in electric field formed between them, will impede the separation of photogenerated carriers in the $InVO_4/BiVO_4$ heterojunction via the traditional dual-channel charge transfer pathway. Instead, they encourage the recombination of photogenerated electrons in $BiVO_4$ with photogenerated holes in $InVO_4$, facilitating photogenerated carrier separation according to a Z-scheme transfer mechanism as visualized in Figure 2b. To verify this inference, *in-situ* irradiated X-ray photoelectron spectroscopy (ISI-XPS) measurements were employed to investigate the photogenerated carrier transfer orientation at the $InVO_4/BiVO_4$ heterojunction interface [38,39]. The results show that the binding energies of In 3d in the $InVO_4/BiVO_4$ shift negatively before and after light irradiation, while the binding energies of Bi 4f shift towards higher binding energy (Figure S11). These photoexcitation-induced changes in elemental binding energies indicate the transfer of photogenerated electrons from $BiVO_4$ to $InVO_4$ in the $InVO_4/BiVO_4$ heterojunction, confirming a Z-scheme charge transfer mechanism for photogenerated carriers in the $InVO_4/BiVO_4$ heterojunction.

To further validate the Z-scheme transfer route of photogenerated carriers in $InVO_4/BiVO_4$ heterojunction, the redox capacities of $InVO_4$, $BiVO_4$ and $InVO_4/BiVO_4$ were examined by radical trapping experiments with 5,5-dimethyl-1-pyrroline-*N*-oxide (DMPO) as the radical trapping agent [40]. As illustrated in Figure 2c, $BiVO_4$ exhibits no detectable DMPO–O_2^- signals after irradiation, due to the insufficient driving force of photogenerated electrons in the conduction band of $BiVO_4$ (E_{CB} = 0.11 V *vs*. SHE) to reduce O_2 to $\cdot O_2^-$ (−0.33 V *vs*. SHE). Compared with $InVO_4$ alone, the significantly enhanced DMPO–O_2^- characteristic peaks were detected in the $InVO_4/BiVO_4$ heterojunction. This observation suggests that the photoelectrons in the conduction band of $InVO_4$ in the $InVO_4/BiVO_4$ heterojunction are greatly retained and not transferred to the conduction band of $BiVO_4$. Meanwhile, significant DMPO–OH signals were detected for $BiVO_4$; however, no characteristic signals of DMPO–OH were observed for $InVO_4$ as presented in Figure 2d, because the valence band of $InVO_4$ (E_{VB} = 1.53 V *vs*. SHE) has a more negative oxidation potential relative to the oxidation of H_2O to ·OH radicals. However, stronger DMPO–OH signals can be observed for the $InVO_4/BiVO_4$ heterojunction, implying that the photogenerated holes in the $BiVO_4$ valence band are well preserved rather than transferred to the valence band of $InVO_4$. These results further demonstrate the Z-scheme charge transfer mechanism in the $InVO_4/BiVO_4$ heterojunction. Therefore, the photogenerated electrons in the conduction band of $InVO_4$ and the photogenerated holes in the valence band of $BiVO_4$ remained,

which endow the $InVO_4/BiVO_4$ heterojunction with strong redox capacities.

2.3 Photocatalytic methane oxidation performance

The photocatalytic activities of various catalysts towards CH_4 oxidation were evaluated in a specifically designed circulating flow system operated at room temperature and atmospheric pressure, using atmospheric oxygen as the oxidant (Figure S12). It is worth noting that the flow system allows a better separation of the oxidation products to prevent their excessive oxidation [13]. As depicted in Figure 3a, no significant oxidation products are observed using $InVO_4$ as the photocatalyst, which is attributed to the insufficient oxidative capacity of the photogenerated holes in $InVO_4$. The pristine $BiVO_4$ exhibits poor photocatalytic CH_4 oxidation activity, with the yield of oxidation products (CH_3OH, HCHO) being only 66.2 μmol g^{-1} h^{-1}, and the selectivity being 87.7%. Notably, the photocatalytic CH_4 oxidation activity of $InVO_4/BiVO_4$ composites prepared through a cation-exchange strategy is significantly enhanced. The optimal photocatalytic yield for CH_4 oxidation to oxygenated hydrocarbons reaches 318.9 μmol g^{-1} h^{-1} with a selectivity of 94.5%, which is 4.8 times higher than that of $BiVO_4$ alone. Compared with other reported catalysts under similar mild conditions, the $InVO_4/BiVO_4$ heterojunction prepared in this work exhibits good performance in the photocatalytic oxidation of methane to oxygenates (Table S1, Supporting Information online). Additionally, the $InVO_4$:$BiVO_4$ catalyst was further prepared by the traditional electrostatic self-assembly method for comparison (see details in the Experimental section). The measurement results reveal that the photocatalytic CH_4 oxidation activity of the $InVO_4$:$BiVO_4$ catalyst is not significantly improved compared to pristine $BiVO_4$. These findings suggest that the *in-situ* cation-exchange strategy provides the $InVO_4/BiVO_4$ Z-scheme heterojunction with a more closely contacted interface, thus ensuring effective charge separation efficiency and excellent redox capability, both of which are crucial for improving the photocatalytic efficiency.

The stability of the $InVO_4/BiVO_4$ heterojunction catalyst was further investigated by continuous irradiation reaction in the circulating flow reactor system. As shown in Figure 3b, the catalyst can maintain excellent catalytic activity over 30 h, yielding oxygenated hydrocarbons at a rate of 8230 μmol g^{-1} with a selectivity exceeding 90%. Moreover, the yields of photocatalytic reaction products exhibit only a slight decrease after 7 repeated experiments (Figure S13), which confirms the stability of the catalyst. Further comparison of the XRD spectra before and after the reaction shows that the characteristic diffraction peaks of the components remain basically unchanged (Figure S14), suggesting that the crystal structure of the catalyst is not affected during the reaction process. In addition, the SEM measurement results show that the morphology and size of $InVO_4/BiVO_4$ after the photocatalytic reaction have hardly changed

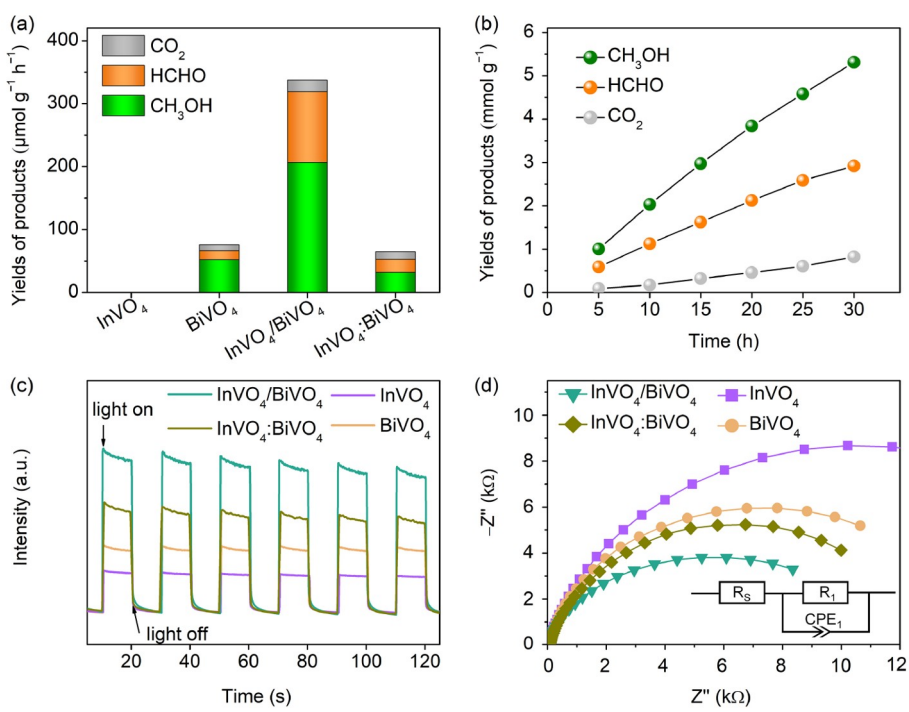

Figure 3 (Color online) (a) Yields of products with different photocatalysts in the circulating flow system, reaction conditions: 10 mg photocatalyst, the mixture of CH_4 and air (gas ratio of CH_4/air: 10/1) at a flow rate of 20 mL min^{-1}, 3 h of 300 W Xe lamp ($\lambda \geqslant 400$ nm) irradiation at room temperature with a light intensity of 200 mW cm^{-2}. (b) Time-on-line amounts of products by $InVO_4/BiVO_4$. *I-t* curves (c) and EIS Nyquist plots (d) of different photocatalysts.

compared to those of $InVO_4/BiVO_4$ before the reaction (Figure S15). All of the above experimental evidence fully demonstrates the excellent photocatalytic stability of the $InVO_4/BiVO_4$ composites prepared in this work.

In addition, the relationship between the photogenerated carrier separation efficiency and catalytic performance of $InVO_4/BiVO_4$ composite was further investigated by employing transient photocurrent response (*I-t*) and electrochemical impedance spectroscopy (EIS) measurements. The *I-t* curves show that the photocurrent density of $InVO_4/BiVO_4$ composite is significantly higher than that of $InVO_4$ or $BiVO_4$ (Figure 3c), indicating that the photogenerated carriers transport efficiency of the heterojunction composite is greatly improved. The EIS measurements demonstrate that the charge transfer resistance of the composite is significantly smaller than those of the two single components (Figure 3d, Table S2), indicating that the *in-situ* conversion of $BiVO_4$ on $InVO_4$ can effectively separate the charges and lead to a reduced charge transfer resistance. These results illustrate again that the structure of the $InVO_4/BiVO_4$ Z-scheme heterojunction composite not only enhances its oxidation and reduction capabilities, but also improves the photogenerated carrier transport efficiency, which is the microscopic origin of the enhanced photocatalytic performance. It is noteworthy that $InVO_4/BiVO_4$ also exhibits a bigger photocurrent density and smaller charge transfer resistance than $InVO_4$:$BiVO_4$, and this is consistent with its enhanced photocatalytic activity, suggesting that $InVO_4/BiVO_4$ has a higher separation and transport efficiency of photogenerated carriers owing to the close contact interface, which is the key factor contributing to the enhancement of the photocatalytic activity.

2.4 Mechanism of photocatalytic methane oxidation

Herein, a feasible mechanism of the photocatalytic CH_4 oxidation based on the $InVO_4/BiVO_4$ heterojunction is proposed in Figure 4. Specifically, the photogenerated carriers in the $InVO_4/BiVO_4$ heterojunction are transported following a Z-scheme mechanism, where the photogenerated holes in the valence band of $InVO_4$ are annihilated by the photogenerated electrons in the conduction band of $BiVO_4$. The photogenerated holes in the $BiVO_4$ valence band oxidize H_2O to generate ·OH radicals, which are key reactive species for activating the C–H bonds of CH_4 to generate $\cdot CH_3$ radicals. The obtained $\cdot CH_3$ radicals then can form CH_3OOH through combining with protons and O_2 (or the $\cdot O_2^-$ radicals generated from photoelectron reduction of O_2). Due to the inherent instability, the CH_3OOH will undergo intramolecular photolytic dehydration to form HCHO or be further reduced to CH_3OH by photogenerated electrons. Another source of CH_3OH is the direct coupling of the produced $\cdot CH_3$ and ·OH radicals. Furthermore, the oxidation product CH_3OH can be

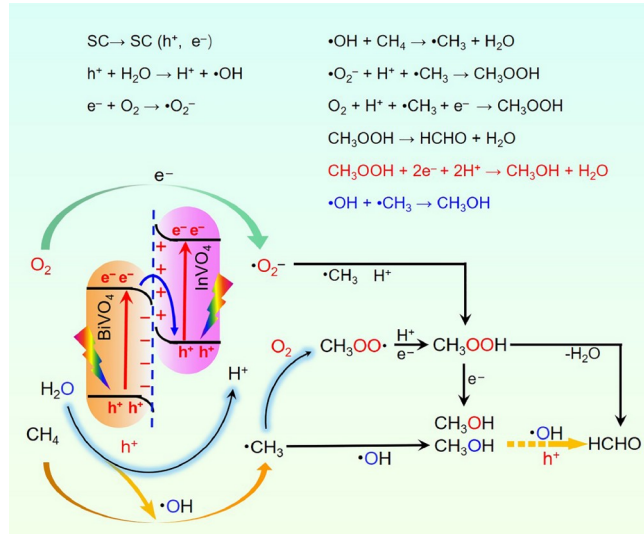

Figure 4 (Color online) Schematic diagram of the proposed reaction pathway for CH_4 conversion with $InVO_4/BiVO_4$ as the photocatalyst.

further oxidized to HCHO by ·OH radicals or photogenerated holes, representing an alternative pathway for HCHO production.

The origin of ·OH radicals can be confirmed through a series of control experiments conducted using fluorescent probe molecules (coumarin) [41]. As demonstrated in Figure S16, the generation of ·OH radicals is undetectable in the absence of either $BiVO_4$ or H_2O. In contrast, when both $BiVO_4$ and H_2O are present, a bright fluorescent signal resulting from the combination of the fluorescent probe molecules with ·OH radicals is clearly observable. Furthermore, the disappearance of the ·OH radical signal is apparent when triethylamine (Et_3N) is used as the photogenerated hole annihilator in the $BiVO_4$ and H_2O reaction system. Based on the above experimental results, it can be preliminarily determined that the ·OH radicals originate from the oxidation of H_2O by the photogenerated holes of $BiVO_4$. Additionally, it is clearly evident that the fluorescence signal is significantly enhanced when the air in the reaction system is replaced by pure O_2, indicating that the presence of O_2 has a prominent promotion effect on the generation of ·OH radicals (Figure S17). Notably, the fluorescence signal of ·OH radicals is further enhanced by using Ag^+ ions as the electron annihilator instead of O_2. It can be inferred that the enhanced fluorescence signal in the O_2 atmosphere is not a result of the reduction of O_2 to ·OH radicals, but rather due to the presence of O_2 consuming the photogenerated electrons and promoting the photogenerated carrier separation, which in turn leads to a higher efficiency of photogenerated holes in oxidizing H_2O to produce ·OH radicals. The origin of the ·OH radicals was further determined by isotope labeling experiments. It is distinctly apparent that only 7-^{18}OH-coumarin (m/z = 164) is observed when $^{16}O_2$ and $H_2{}^{18}O$ as

feedstocks (Figure 5a), demonstrating that the ·OH radicals do indeed originate from the oxidation of H_2O rather than from the photoreduction of O_2.

The mechanism of C–H bond oxidation was investigated by radical trapping experiments using DMPO as a radical trapping agent. As illustrated in Figure 5b, when H_2O is the only absent component in the detection system, no radical signal can be detected, indicating that the photogenerated holes are insufficient to activate C–H bonds. When H_2O is present but CH_4 is absent, the DMPO–OH signal becomes clearly visible. It is noteworthy that when the system contains both H_2O and CH_4, the signals of DMPO–OH and DMPO–CH_3 can be detected simultaneously [42]. In addition, the signals of ·CH_3 radicals are gradually enhanced with increasing irradiation time, while the signals of ·OH radicals are weakened, which is mainly attributed to the fact that the ·OH radicals consume their own quantity while oxidizing CH_4 to produce ·CH_3 radicals. Furthermore, the radical signal intensities of the $InVO_4/BiVO_4$ catalyst system are stronger than those of $BiVO_4$ alone, which is consistent with the photocatalytic activity results, indicating that the ·OH radical plays a critical role in the CH_4 activation process. Based on the above evidence, it is suggested that the C–H bonds of CH_4 are activated via H-abstraction by ·OH radicals.

The origin of the oxidation product CH_3OH was further explored to elucidate the process of CH_3OH generation. Firstly, isotopic labeling experiments combined with mass spectrum analysis were conducted to determine the carbon source of the oxidation product. As shown in Figure 5c, the characteristic peaks of $^{13}CH_3OH$ (m/z = 33) can be clearly observed in the mass spectrum when $^{13}CH_4$ is used as the raw material, whereas only $^{12}CH_3OH$ (m/z = 32) is detected when $^{12}CH_4$ is used as the feedstock. Moreover, distinct splitting peaks (δ = 3.12 and 3.40 ppm) belonging to $^{13}CH_3OH$ can be observed in the proton nuclear magnetic resonance (^{1}H NMR) spectrum of the $^{13}CH_4$ system (Figure S18) [43]. These results confirm that the carbon source of the oxidation product CH_3OH is derived from CH_4. Thereafter, the reaction paths of O_2 and H_2O were verified by examining the source of oxygen in the oxidation products. It can be clearly observed that $CH_3{}^{18}OH$ (m/z = 34) is the main product when $^{18}O_2$ and $H_2{}^{16}O$ are used as feedstocks, whereas the main product is $CH_3{}^{16}OH$ (m/z = 32) accompanied by a small amount of $CH_3{}^{18}OH$ (m/z = 34) when $^{16}O_2$ and $H_2{}^{18}O$ are used (Figure S19). This indicates that the source of oxygen for the oxidation product CH_3OH is primarily derived from O_2 and partially from H_2O. Furthermore, the response mechanism of O_2 molecules was examined by employing EPR measurements. In the system with H_2O and CH_4, only significant ·OH and ·CH_3 radical signals are detected. Upon introducing O_2 into the system, it is observed that the CH_3OO· radical signals are generated (Figure 5d) [44]. Therefore, it can be inferred that O_2 reacts with the ·CH_3 radicals to form the CH_3OO· radicals, and these CH_3OO· radicals then combine with protons aided by electrons to form the

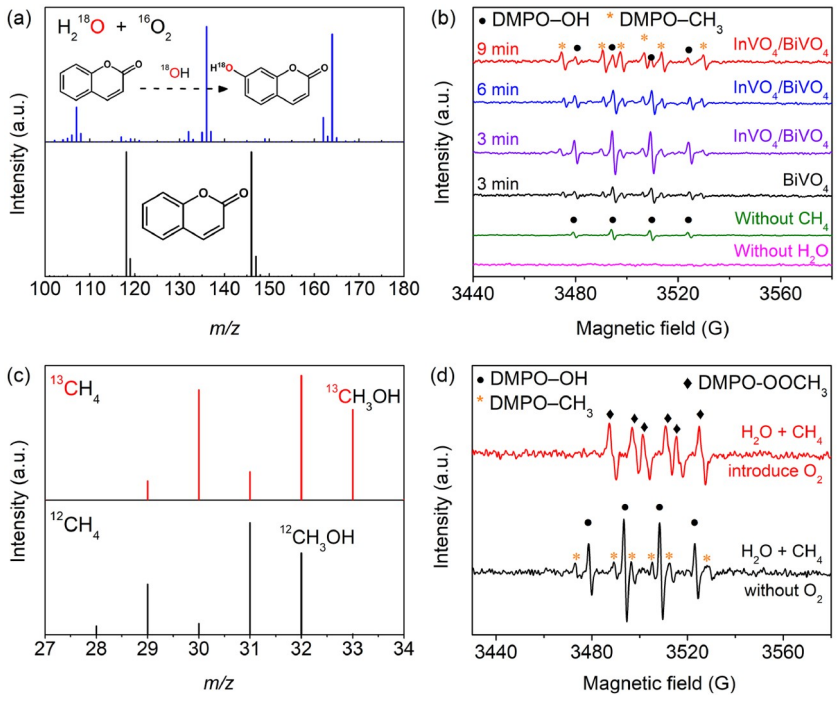

Figure 5 (Color online) (a) Mass spectra of 7-OH-coumarin generated over $InVO_4/BiVO_4$ with $^{16}O_2$ + $H_2{}^{18}O$ as feedstocks. (b) Comparison of EPR intensities of DMPO–OH and DMPO–CH_3 for various photocatalysts at different reaction times. (c) Mass spectra of CH_3OH generated over $InVO_4/BiVO_4$ from $^{13}CH_4$ (top) and $^{12}CH_4$ oxidation (below). (d) EPR spectra of DMPO–OH, DMPO–CH_3, and DMPO–$OOCH_3$ before and after the introduction of O_2 in the photocatalytic oxidation of CH_4.

CH_3OOH intermediate. The presence of CH_3OOH can be confirmed by ^{13}C NMR spectrum (Figure S20). No significant CH_3OOH product can be detected in this reaction system because it is very easily reduced to CH_3OH by photogenerated electrons [45].

The above inferences were fully validated by further control experiments with the annihilating active species (Figure S21). First, almost no oxidation product was detected in the reaction system without H_2O participation. When Et_3N and isopropanol (IPA) were utilized to annihilate the photogenerated holes and ·OH radicals, respectively, there was a substantial reduction in the amount of the oxidation products in the reaction system, implying that the ·OH radicals generated through the oxidation of H_2O by photogenerated holes are the key active species for driving the CH_4 oxidation reaction. Additionally, the production of oxidation products was almost completely inhibited when the $\cdot CH_3$ radicals were annihilated using TEMPO, suggesting that $\cdot CH_3$ is an important intermediate during the generation of oxidation products. When the $\cdot O_2^-$ radicals were annihilated by the benzoquinone (PBQ), the generation of the oxidation products was slightly inhibited, implying a non-negligible role of $\cdot O_2^-$ in the product formation. After annihilating the photogenerated electrons using Ag^+ ions in the absence of O_2, a small amount of oxidation product was still produced, inferring that a direct coupling reaction occurs between $\cdot CH_3$ and ·OH radicals to produce CH_3OH, which is consistent with the mass spectrum showing that the oxygen source of the oxidation product is partly derived from H_2O. In the absence of O_2 and Ag^+ during the reaction, almost no oxidation product was detectable. It suggests there is an indispensable role for O_2 to consume photogenerated electrons in promoting the oxidation of H_2O by photogenerated holes to produce ·OH radicals to activate the C–H bonds of CH_4, in addition to its participation in the generation of oxidation products.

3 Conclusions

In summary, a robust and environmentally friendly $InVO_4$/$BiVO_4$ Z-scheme heterojunction was successfully constructed by decorating $BiVO_4$ onto $InVO_4$ via a simple cation-exchange strategy, combined with an *in-situ* transformation technology. Structural characterization and XPS measurements unveiled that the *in-situ* growth method endows the $InVO_4$/$BiVO_4$ heterojunction with strong interfacial electronic coupling, which significantly accelerates the interfacial charge transfer and enhances the separation efficiency of photogenerated carriers via the Z-scheme pathway, as evidenced by ISI-XPS, EPR and photoelectrochemical measurements. Consequently, the $InVO_4$/$BiVO_4$ heterojunction exhibits superior performance in the photocatalytic CH_4 conversion reaction, achieving an oxygenated hydrocarbon yield of 318.9 μmol g^{-1} h^{-1} and a selectivity of 94.5%, far outperforming both pristine $BiVO_4$ and $InVO_4$: $BiVO_4$ counterpart prepared via electrostatic self-assembly. Furthermore, comprehensive control experiments, isotope labeling experiments, and EPR measurements disclosed that CH_4 activation occurs through hydrogen abstraction by ·OH radicals generated from the oxidation of water by photogenerated holes, and the key intermediate CH_3OOH is primarily formed through the combination of $\cdot CH_3$ radicals with O_2 and protons.

Acknowledgements This work was supported by the National Key R&D Program of China (2022YFA1502902), the National Natural Science Foundation of China (22475152, U21A20286) and the 111 Project of China (D17003).

Conflict of interest The authors declare no conflict of interest.

Supporting information The supporting information is available online at http://chem.scichina.com and http://link.springer.com/journal/11426. The supporting materials are published as submitted, without typesetting or editing. The responsibility for scientific accuracy and content remains entirely with the authors.

1 Li X, Li C, Xu Y, Liu Q, Bahri M, Zhang L, Browning ND, Cowan AJ, Tang J. *Nat Energy*, 2023, 8: 1013–1022
2 Li Q, Ouyang Y, Li H, Wang L, Zeng J. *Angew Chem Int Ed*, 2022, 61: e202108069
3 Zhou P, Tang S, Ye Z, Navid IA, Xiao Y, Sun K, Mi Z. *Chem Sci*, 2024, 15: 1505–1510
4 Zhang C, Wang J, Ouyang S, Song H, Ye J, Shi L. *Sci China Chem*, 2023, 66: 2532–2557
5 Fletcher SEM, Schaefer H. *Science*, 2019, 364: 932–933
6 Blankenship A, Artsiusheuski M, Sushkevich V, van Bokhoven JA. *Nat Catal*, 2023, 6: 748–762
7 Huang Q, Cai J, Wei F, Fan Y, Liang Z, Liu K, Lu XF, Ding Z, Wang S. *J Mater Chem A*, 2024, 12: 21334–21340
8 Meng X, Cui X, Rajan NP, Yu L, Deng D, Bao X. *Chem*, 2019, 5: 2296–2325
9 Xu Y, Wang C, Li X, Xiong L, Zhang T, Zhang L, Zhang Q, Gu L, Lan Y, Tang J. *Nat Sustain*, 2024, 7: 1171–1181
10 Song H, Meng X, Wang Z, Liu H, Ye J. *Joule*, 2019, 3: 1606–1636
11 Xiao Z, Wan Z, Zhang J, Jiang J, Li D, Shen J, Dai W, Li Y, Wang X, Zhang Z. *ACS Catal*, 2024, 14: 9104–9114
12 Wang J, Peng Y, Xiao W. *Sci China Chem*, 2023, 66: 3252–3261
13 Dong GX, Zhang MR, Su K, Liu ZL, Zhang M, Lu TB. *J Mater Chem A*, 2023, 11: 9989–9999
14 Li X, Wang C, Tang J. *Nat Rev Mater*, 2022, 7: 617–632
15 Hu W, Sun Y, Li S, Cheng X, Cai X, Chen M, Zhu Y. *CCS Chem*, 2021, 3: 2509–2519
16 Gunsalus NJ, Koppaka A, Park SH, Bischof SM, Hashiguchi BG, Periana RA. *Chem Rev*, 2017, 117: 8521–8573
17 Wang K, Luo L, Wang C, Tang J. *Chin J Catal*, 2023, 46: 103–112
18 Dhandole LK, Kim SH, Moon G. *J Mater Chem A*, 2022, 10: 19107–19128
19 Zhang R, Shi J, Fu L, Liu YG, Jia Y, Han Z, Yuan K, Jiang HY. *ACS Nano*, 2024, 18: 12994–13005
20 Zhang C, Yan Y, Huang H, Peng X, Song H, Ye J, Shi L. *ACS Catal*, 2023, 13: 15351–15359
21 Bo C, Zhang L, Liu X, Chang H, Sun Y, Zhang X, Tan T, Piao L. *Nano Res*, 2024, 17: 2473–2480

22 Wang P, Shi R, Zhao Y, Li Z, Zhao J, Zhao J, Waterhouse GIN, Wu L, Zhang T. *Angew Chem Int Ed*, 2023, 62: e202304301
23 Fan Y, Jiang Y, Lin H, Li J, Xie Y, Chen A, Li S, Han D, Niu L, Tang Z. *Nat Commun*, 2024, 15: 4679
24 Luo L, Gong Z, Xu Y, Ma J, Liu H, Xing J, Tang J. *J Am Chem Soc*, 2022, 144: 740–750
25 Zheng K, Wu Y, Zhu J, Wu M, Jiao X, Li L, Wang S, Fan M, Hu J, Yan W, Zhu J, Sun Y, Xie Y. *J Am Chem Soc*, 2022, 144: 12357–12366
26 Fan Y, Zhou W, Qiu X, Li H, Jiang Y, Sun Z, Han D, Niu L, Tang Z. *Nat Sustain*, 2021, 4: 509–515
27 Zhang P, Li J, Huang H, Sui X, Zeng H, Lu H, Wang Y, Jia Y, Steele JA, Ao Y, Roeffaers MBJ, Dai S, Zhang Z, Wang L, Fu X, Long J. *J Am Chem Soc*, 2024, 146: 24150–24157
28 Yu D, Jia Y, Yang Z, Zhang H, Zhao J, Zhao Y, Weng B, Dai W, Li Z, Wang P, Steele JA, Roeffaers MBJ, Dai S, Huang H, Long J. *ACS Sustain Chem Eng*, 2022, 10: 16–22
29 Pan F, Xiang X, Du Z, Sarnello E, Li T, Li Y. *Appl Catal B-Environ*, 2020, 260: 118189
30 Yu X, Zholobenko VL, Moldovan S, Hu D, Wu D, Ordomsky VV, Khodakov AY. *Nat Energy*, 2020, 5: 511–519
31 Song H, Meng X, Wang S, Zhou W, Wang X, Kako T, Ye J. *J Am Chem Soc*, 2019, 141: 20507–20515
32 Murcia-López S, Villa K, Andreu T, Morante JR. *Chem Commun*, 2015, 51: 7249–7252
33 Wang C, Xu Y, Tang J. *Sci China Chem*, 2023, 66: 1032–1051
34 Liu ZL, Luo HY, Zhang MR, Mu YF, Bai FQ, Zhang M, Lu TB. *Chem Eng J*, 2024, 491: 151913
35 Yang Q, Tan G, Yin L, Liu W, Zhang B, Feng S, Bi Y, Liu Y, Liu T, Wang Z, Ren H, Xia A. *Chem Eng J*, 2023, 467: 143450
36 Kumar A, Prajapati PK, Pal U, Jain SL. *ACS Sustain Chem Eng*, 2018, 6: 8201–8211
37 Lee D, Wang W, Zhou C, Tong X, Liu M, Galli G, Choi KS. *Nat Energy*, 2021, 6: 287–294
38 Low J, Yu J, Jaroniec M, Wageh S, Al-Ghamdi AA. *Adv Mater*, 2017, 29: 1601694
39 Low J, Dai B, Tong T, Jiang C, Yu J. *Adv Mater*, 2019, 31: 1802981
40 Zhang W, Mohamed AR, Ong W. *Angew Chem Int Ed*, 2020, 59: 22894–22915
41 Xiang Q, Yu J, Wong PK. *J Colloid Interface Sci*, 2011, 357: 163–167
42 Ab Rahim MH, Forde MM, Jenkins RL, Hammond C, He Q, Dimitratos N, Lopez-Sanchez JA, Carley AF, Taylor SH, Willock DJ, Murphy DM, Kiely CJ, Hutchings GJ. *Angew Chem Int Ed*, 2013, 52: 1280–1284
43 Agarwal N, Freakley SJ, McVicker RU, Althahban SM, Dimitratos N, He Q, Morgan DJ, Jenkins RL, Willock DJ, Taylor SH, Kiely CJ, Hutchings GJ. *Science*, 2017, 358: 223–227
44 Jiang Y, Fan Y, Li S, Tang Z. *CCS Chem*, 2023, 5: 30–54
45 Bañares MA, Alemany LJ, López Granados M, Faraldos M, Fierro JLG. *Catal Today*, 1997, 33: 73–83